

# The Physical Interpretation of X-ray Phase Lags and Coherence: RXTE Observations of Cygnus X-1 as a Case Study

M.A. Nowak<sup>a</sup>, J.B. Dove<sup>b</sup>, B.A. Vaughan<sup>c</sup>, J. Wilms<sup>a,d</sup>, and M.C. Begelman<sup>a,e</sup>

<sup>a</sup>JILA, Campus Box 440, Boulder, CO 80309-0440, USA

<sup>b</sup>Dept. of Physics and Astronomy, University of Wyoming, Laramie, WY 82071, USA

<sup>c</sup>Space Radiation Lab, California Institute of Technology, 220-47 Downs, Pasadena, CA 91125, USA

<sup>d</sup>IAA, Abt. Astronomie, Waldhäuser Str. 64, D-72076 Tübingen, Germany

<sup>e</sup>Dept. of APS, University of Colorado, Boulder, CO 80309, USA

There have been a number of recent spectral models that have been successful in reproducing the observed X-ray spectra of galactic black hole candidates (GBHC). However, there still exists controversy over such issues as: what are the sources of hard radiation, what is the system's geometry, is the accretion efficient or inefficient, etc. A potentially powerful tool for distinguishing among these possibilities, made possible by the *Rossi X-ray Timing Explorer (RXTE)*, is the variability data, especially the observed phase lags and variability coherence. These data, in conjunction with spectral modeling, have the potential of determining physical sizes of the system, as well as placing strong constraints on both Compton corona and advection models. As an example, we present *RXTE* variability data of Cygnus X-1.

## 1. INTRODUCTION

Many black hole candidate (BHC) systems show three or more spectral states: the “low” (X-ray hard), “high” (X-ray soft), and “very high” (X-ray soft, plus a hard, power-law tail) states. Typically, sources are seen to be in the low state when they are below  $\sim 10\%$  of their Eddington luminosity, and they tend to exist in the high and very high states at observed luminosities above  $10\% L_{\text{Edd}}$  [1]. In this article, we will concentrate on the properties of the low state, for which we have obtained  $\sim 20$  ks of Cyg X-1 data with the *Rossi X-ray Timing Explorer (RXTE)* [2,3].

A variety of models have been proposed for the low state of BHC in general, and for the low state of Cyg X-1 in specific. Currently, these models fall into two main classes: the Compton corona models [2–9] and the Advection Dominated Accretion Flow (ADAF) models [10,11]. For the Compton corona models, the currently favored geometry is one in which a central, spherical corona is surrounded by an exterior, cold

disk [2,3,6–9]. This is similar to the geometry proposed by the ADAF models [10,11]; however, the ADAF models invoke different sources for the Comptonization seed photons<sup>1</sup>, and they make more detailed predictions for the dynamics of the inner region. Specifically, the advective inner region is moving quasi-radially, at close to the free-fall velocity, toward the black hole.

We note that Cyg X-1 has upon occasion, including very recently, transitioned to the high state [12]. Different scenarios have been proposed for this transition in both the Compton corona picture [9] and the ADAF picture [11]. We will not discuss this transition here. Instead, we will concern ourselves with how variability data, i.e. the phase/time lags and the coherence function, can be used to constrain models within a given state. As described below, these data currently pose challenges for both the Compton corona and ADAF models of the low state.

---

<sup>1</sup>ADAFs take the Comptonization seed photons to be cylo/synchrotron photons generated within the advective region itself.

## 2. SPECTRAL MODEL OF CYG X-1

As an example of a successful (in terms of fitting the energy spectra) low state model, we consider the spherical corona model of Dove et al. [7,8,2,3]. Its basic features are as follows. The inner region of the accretion system is modeled as a spherical cloud with total optical depth  $\sim 1.6$  and an *average* temperature of 87 keV. This spherical region is then surrounded by a cold ( $T \leq 150$  eV), geometrically thin disk which reprocesses hard radiation from the corona, as well as provides seed photons for Comptonization. The overall quality of the fit of this model to our Cyg X-1 data is quite good ( $\chi_{\text{red}}^2 = 1.6$ ). We will use this as our “straw man” model when we discuss the limits that phase lags place on coronal models (§4.4).

## 3. POWER SPECTRAL DENSITY

The power spectral density (PSD) is calculated by taking lightcurves from the data, dividing them into segments of equal length, and then taking the Fast Fourier Transform (FFT) of each data segment. The squared amplitude of each individual FFT (for a given lightcurve) is then averaged together. Furthermore, we usually average over (logarithmically spaced) Fourier frequency bins as well. This yields the resulting PSD for each lightcurve. Here we choose a normalization such that the integral of the PSD over Fourier frequency yields the *square* of the total *root mean square (rms) amplitude* of the variability [13]. For a given narrow Fourier frequency interval, the rms is (to within a factor of  $\sqrt{2}$ ) the fractional amount by which the lightcurve is sinusoidally modulated in that given frequency interval.

In Figure 1 we plot the PSD of the low energy band (0 – 3.86 keV) for our Cyg X-1 data. This PSD, in both shape and amplitude, is very similar to what has been previously observed. We note, however, that there is a weak, broad feature at 0.005 Hz, with rms  $\sim 1.5\%$ . A Lomb-Scargle periodogram [14] indicates that the significance of this feature is  $\sim 50\%$ . However, for reasons discussed in §5, this feature may be somewhat more significant than that.

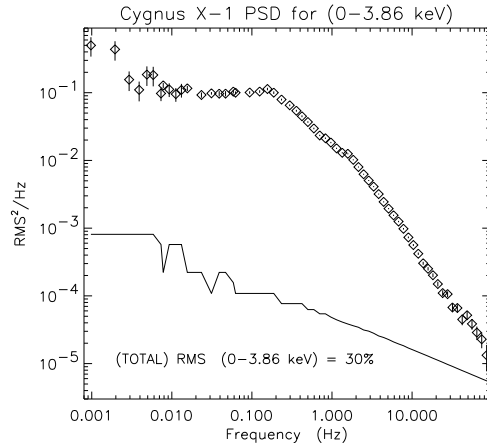


Figure 1. Power Spectral Density of the (0-3.86 keV) band of Cyg X-1. The solid line corresponds to the “effective” noise level. For the normalization of Miyamoto [13], this is  $2/(\text{Count Rate})$ , divided by the number of FFTs and frequency bins averaged over. FFTs for lightcurves of 1024, 128, and 32 s duration were combined for this plot.

## 4. PHASE LAGS

### 4.1. Basics

Fourier phase lags (and equivalently Fourier time lags) are calculated from the FFTs constructed from data segments of two different, but concurrent, lightcurves. Let  $s(t)$  be a “soft energy” light curve and  $h(t)$  be a “hard energy” lightcurve. The Fourier phase lag,  $\phi(f)$ , is then just the phase of the (complex) quantity

$$\langle S^*(f)H(f) \rangle, \quad (1)$$

where  $S(f)$  and  $H(f)$  are the FFTs of the concurrent data segments of  $s(t)$  and  $h(t)$ , respectively. The \* denotes a complex conjugate and the angle brackets denote an average over data segments and/or Fourier frequency bins. The time lag,  $\tau(f) \equiv \phi(f)/2\pi f$ .

In general, both the phase lag and time lag are non-constant functions of Fourier frequency,  $f$ . However, we naively expect that the *longest* observed time lag in the system is no longer than the *longest* distance in the system divided by the *slowest* propagation speed. As shown in Fig. 2, this longest time for Cyg X-1 is  $\sim 0.1$  s. This is

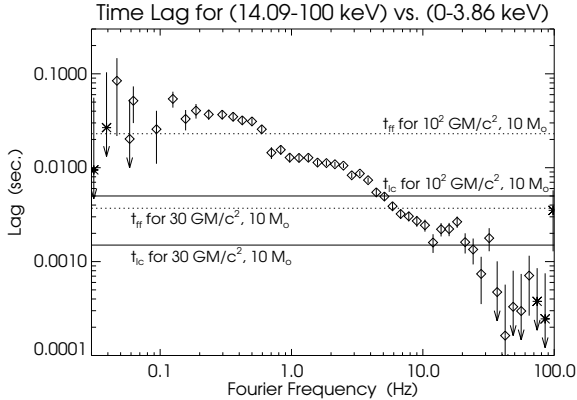


Figure 2. Time lags (as a function of Fourier frequency) in Cyg X-1 for the (14.09 – 100 keV) vs. (0 – 3.86 keV) energy bands. Open diamonds, the hard lags behind the soft; \* the soft lags behind the hard. Horizontal lines are characteristic timescales for a  $10 M_{\odot}$  black hole. Dotted lines are the (radial) free-fall timescales from  $R = 30, 100 GM/c^2$ , and solid lines are the light crossing times for  $R = 30, 100 GM/c^2$ .

considerably longer than both the expected free-fall timescales for ADAF models and the sound travel time of hot corona models. Therefore, these data may pose a problem for both of these models.

Similarly, the *shortest* observed time lag should be longer than the *smallest* scale (over which significant luminosity is generated) divided by the *fastest* propagation speed. As shown in Fig. 2, the shortest time lags observed in Cyg X-1 are comparable to a light crossing time, and therefore may be relevant to determining physical parameters for Compton corona models (cf. §4.4).

If the coherence function is unity (cf. §5), one can often think of the phase lag in terms of a transfer function. For this case, we have  $H(f) = A(f) \exp[i\phi(f)]S(f)$ , where  $A(f)$  is a real-valued amplitude. In the time domain, this means that  $h(t)$  is the convolution of  $s(t)$  with a *linear* transfer function. Specifically,

$$h(t) = \int_{-\infty}^{\infty} t_r(t - \tau) s(\tau) d\tau .$$

The Fourier transform of  $t_r(\tau)$  is then just  $A(f) \exp[i\phi(f)]$ .

## 4.2. Simple Interpretations

Imagine that we have a source of fluctuations that produces soft X-ray photons that is some distance from a region that produces hard X-ray photons. If the disturbances can propagate from the soft photon producing region to the hard photon producing region—without dispersion—then we expect there to be a time delay between the soft and hard photons that is *independent of Fourier frequency,  $f$* . The time delay at all Fourier frequencies will simply be the distance between the soft X-ray source and the hard X-ray response divided by the propagation speed. This means that the Fourier phase lag will increase linearly with  $f$  (modulo integer multiples of  $2\pi$ ).

As shown in Fig. 2, the time lags observed in Cyg X-1 are not independent of Fourier frequency. If anything, the Fourier phase lag is more approximately independent of  $f$ . A crude, but illustrative, model of this is as follows. If  $H(f)$  is the transform of the hard photon light curve and  $S(f)$  is the transform of the soft photon light curve, let

$$H(f) = A \exp(\pm i\Delta\phi) S(f) , \quad (2)$$

where both  $A$  and  $\Delta\phi$  are constants, and the  $+$  is for  $f > 0$  and the  $-$  is for  $f < 0$ . [The antisymmetry in the relative phase is due to the fact that real light curves produce Fourier transforms where  $H(f) = H^*(-f)$ .] Taking the inverse transform of  $A \exp(\pm i\Delta\phi)$ , the transfer function,  $t_r(\tau)$ , can be written in the time domain as

$$t_r(\tau) = A \left[ \cos(\Delta\phi) \delta(\tau) + \frac{\sin(\Delta\phi)}{\tau} \right] . \quad (3)$$

That is, a fraction  $A \cos(\Delta\phi)$  of the hard variability is *exactly* coincident with the soft variability, while a (typically smaller) fraction is delayed from the soft variability with a  $\tau^{-1}$  “tail” in the transfer function. For  $A \sim 1$  and  $\Delta\phi \sim 0.1$  radians, roughly 90% of the soft and hard lightcurves are exactly coincident with one another.

## 4.3. Simple Propagation Models

It is often convenient to think of propagating disturbances in terms of sources and responses.

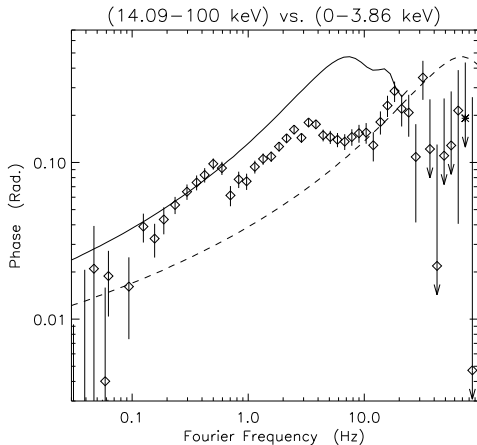


Figure 3. Phase lags (radians) for the data presented in Fig. 2. Lines correspond to the simple propagation model of §4.3. The solid line is for  $c_p \approx 0.01 c$ , and the dashed line is for  $c_p \approx 0.1 c$ , where  $c$  is the speed of light.

For example, we might have a disturbance,  $\Psi(\vec{x}, t)$  that obeys a wave equation

$$\left( \frac{\partial^2}{\partial \vec{x}^2} - c_p^{-2} \frac{\partial^2}{\partial t^2} \right) \Psi(\vec{x}, t) = -4\pi \rho_D(\vec{x}, t), \quad (4)$$

where  $\rho_D(\vec{x}, t)$  is the source of the disturbance.

Imagine that the source of fluctuations,  $\rho_D$ , is separable in space and time. Let us also assume that the *observed* soft X-ray light curve is equal to the disturbance,  $\Psi$ , times a weighting function,  $g_s(\vec{x})$ , integrated over the system. Likewise, let us assume that the *observed* hard X-ray light curve is related to  $\Psi$  via a weighting function  $g_h(\vec{x})$ .

As was discussed by Vaughan & Nowak [15], it is relatively straightforward to calculate the resultant phase lags for this case. Furthermore, the resultant “transfer function” between the soft and hard lightcurves has many of the qualitative properties discussed in §4.2.

As a simple example, let us consider the (phenomenological) weighting functions:

$$\begin{aligned} g_s(r) &\propto \theta\left(\frac{r}{r_0} - 6\right) * \exp\left(-\alpha_s \frac{r}{r_0}\right), \\ g_h(r) &\propto \theta\left(\frac{r}{r_0} - 6\right) * \exp\left(-\alpha_h \frac{r}{r_0}\right), \end{aligned} \quad (5)$$

where  $-\alpha_s$  and  $-\alpha_h$  are constants, and  $\theta$  represents a step function. Here we shall take  $\alpha_s = 0.31$  and  $\alpha_h = 0.58$ , so that the response of the soft X-rays is predominantly at  $r \lesssim 15 r_0$  and the response of the hard X-rays is predominantly at  $r \lesssim 8 r_0$ . For the case of Cyg X-1, we will take  $r_0 = 6 GM/c^2$  with  $M = 10 M_\odot$ . The resultant phase lags then depend upon  $c_p$ , the propagation speed of the disturbances (which we take to be uniform, with the waves directed toward a “sink” at the inner disk edge) [15].

As shown in Fig. 3, such a model qualitatively reproduces the observed phase lags. However, to obtain quantitative agreement with the phase lags at low Fourier frequency ( $\sim 0.1$  Hz), a very slow propagation speed of  $c_p \approx 0.01 c$ , where  $c$  is the speed of light, is required. As discussed in §4.1, such a slow speed is much less than both the radial velocity in ADAF models, as well as the sound speed for Compton corona models, and therefore is problematic for both models.

#### 4.4. Comptonization Models

Any *intrinsic* time delays between soft and hard photons for Comptonization seed photons will be modified as the seed photons diffuse through the Compton cloud [16–18]. The greater the observed output energy, the longer the diffusion time through the Compton corona. As has been discussed by Miller [17] and Nowak & Vaughan [18], the *minimum* expected time delay is the difference in the diffusion time for the *observed* hard and *observed* soft photons.

We have calculated this minimum time delay for the Compton corona model discussed in §2, and show this along with the data in Fig. 4. Depending upon whether one identifies the  $\sim 10$ – $30$  Hz time lags or the  $\gtrsim 30$  Hz time lags as the upper limit for such a time lag “shelf”, an *upper* limit to the coronal radius is seen to be  $R \approx 45 GM/c^2$  or  $R \approx 10 GM/c^2$  ( $M = 10 M_\odot$ ), respectively. For either case, such a small radial extent of the corona poses a severe problem for ADAF models, as shown in Fig. 2, which would then have great difficulty explaining the longest time lags. (There still remains the possibility for Compton corona models that the longest time lags are “intrinsic” time lags from the outer cold disk, merely

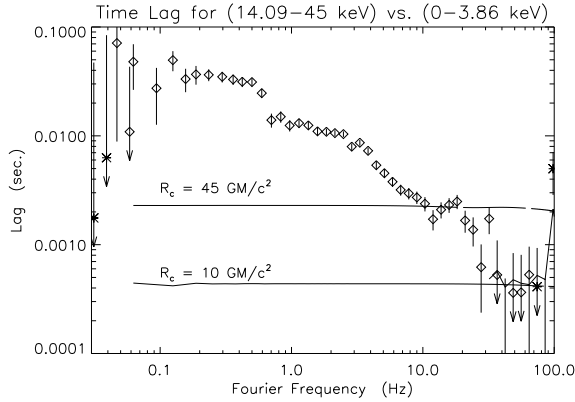


Figure 4. Time lags (as a function of Fourier frequency) for Cyg X-1 data. The solid lines correspond to the *minimum* expected time lag for a spherical Compton corona (with parameters given in §2) of radius  $R = 45 GM/c^2$  and  $R = 10 GM/c^2$  ( $M = 10 M_\odot$ ). Thick line is the magnitude of the Poisson noise limit above 30 Hz.

“reprocessed” by the corona [17,18].)

To be conservative, we identify the 10 – 30 Hz data as the upper limit for the shelf, as the  $> 30$  Hz data shows a strong loss of coherence (cf. Fig 5). We clarify this point below where we describe exactly what we mean by the coherence function.

## 5. COHERENCE FUNCTION

The coherence function has been extensively discussed by Vaughan & Nowak [15]. Essentially, it is the average, normalized amplitude of the cross power spectral density (which is what one is computing to find the time lags). Similar to eq. 1, the coherence function,  $C(f)$  is given by

$$C(f) \equiv \frac{\langle S^*(f)H(f) \rangle^2}{\langle S^2(f) \rangle \langle H^2(f) \rangle} . \quad (6)$$

Various methods exist for determining, and minimizing, the effects of Poisson noise on the estimate of this function [15].

As also discussed by Vaughan & Nowak [15], most previously considered mechanisms for producing variability in BHC systems (i.e. multiple shots or flares, any “nonlinear” processes, etc.)

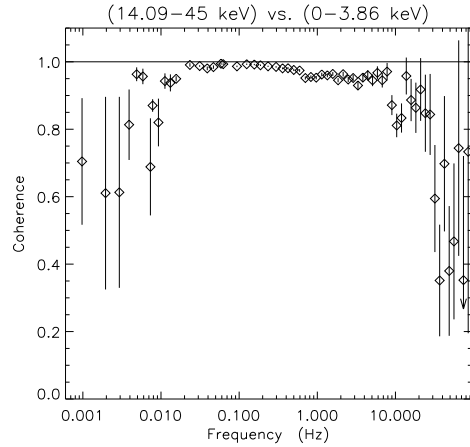


Figure 5. Coherence function (as a function of Fourier frequency) for the data presented in Fig. 2. Note how remarkably close the coherence is to unity in the range  $\sim 0.02 - 10$  Hz. The loss of coherence at frequencies below  $\sim 0.02$  Hz is real, as is the recovery to near unity coincident with the 0.005 Hz feature from Fig. 1. The loss of coherence at high frequency ( $\gtrsim 30$  Hz) may be influenced by uncertainties associated with the Poisson noise level and the instrumental deadtime.

will lead to a strong *loss* of coherence. This makes the near unity coherence shown in Fig. 5 quite remarkable. The near unity coherence seen between  $\sim 0.02 - 10$  Hz argues for a single source of disturbances and/or a global response in Cyg X-1 over (these rather disparate) timescales [15].

In a very real sense, the coherence function is a measurement of the degree of constancy of the phase lags between soft and hard photons as one averages over individual data segments and Fourier frequency bins (as discussed in §4.1). If the phase is constant from data segment to data segment, the coherence is unity. A variable phase, as might be caused by two or more uncorrelated processes relating soft and hard photons, will lead to coherence loss [15]. As the coherence drops rapidly above  $\gtrsim 30$  Hz, we cannot be sure that the observed time lag in this regime is indicative of *solely* the diffusion through a Compton corona. For this reason, we take the 10 – 30 Hz data as the conservative estimate.

Note also that there is a definite loss of coherence below  $\sim 0.02$  Hz. There is a clear trend which is only broken near 0.005 Hz. At that point, there is a recovery of coherence to near unity, coincident with the feature seen in the PSD (cf. Fig. 1). This indicates that, although the Lomb-Scargle periodogram indicated a significance of only 50%, this feature may actually be significant. At the very least, it argues that PSDs of Cyg X-1 should be extended to frequencies as low as  $10^{-3}$  Hz whenever statistics permit.

## 6. SUMMARY

We have discussed the role of Fourier phase/time lags and variability coherence in constraining spectral models of BHC. Much of the theory behind this work can be found in the papers of Dove et al. [7,8], Miller [17], Nowak & Vaughan [18], and Vaughan & Nowak [15]. To illustrate our points, we have presented *RXTE* data of Cyg X-1 (cf. [2,3]).

Despite the general success of spectral models, such as the Compton corona model discussed in §2, the variability data pose substantial challenges. For example, both the ADAF models and Compton corona models (if they rely on sound speed propagation timescales) have substantial difficulty in explaining the longest observed time lags. Explaining the observed unity coherence in Cyg X-1 will be difficult for all models unless they can postulate a *global* variability mechanism.

The shortest observed time lags were also seen to provide upper limits to the size of a spherical Compton corona. The “recovery” to near unity coherence at  $\sim 0.005$  Hz, coincident with a weak feature in the PSD, indicates the possibility of an extremely low frequency oscillation in Cyg X-1.

In short, no currently proposed model for the low state of BHC in general, or the low state of Cyg X-1 in specific, can claim to completely describe both the spectral and variability data. However, with the advent of *RXTE* and *Bep-poSAX*, which between them are capable of broad spectral coverage and fast timing, only models that can explain, or at least be consistent with, both the spectral and variability data should be considered to be viable.

## REFERENCES

1. M.A. Nowak, PASP 718 (1995) 1207.
2. J.B. Dove, J. Wilms, M.A. Nowak, B. Vaughan, M.C. Begelman, MNRAS (in Press) (1998) (astro-ph/9707322).
3. J.B. Dove, M.A. Nowak, J. Wilms, B. Vaughan, this Volume (1998).
4. L. Titarchuk, ApJ 434 (1994) 570.
5. F. Haardt, L. Maraschi, & G. Ghisellini, ApJ 476 (1996) 670.
6. M. Gierliński, et al., MNRAS 288 (1996) 958.
7. J.B. Dove, J. Wilms, M.C. Begelman, ApJ 487 (1997) 747.
8. J.B. Dove, J. Wilms, M.G. Maisack, M.C. Begelman, ApJ 487 (1997) 759.
9. J. Poutanen, J.H. Krolik, & F. Ryde, MNRAS (Submitted) (1997) (astro-ph/9709113).
10. R. Narayan & I. Yi, ApJ 428 (1994) L13.
11. A. Esin, R. Narayan, W. Cui, J.E. Grove, & S.N. Zhang, ApJ, Submitted (astro-ph/971167).
12. W. Cui, S.N. Zhang, W. Focke, & J.H. Swank, ApJ 484 (1997) 383.
13. S. Miyamoto, S. Kitamoto, S. Iga, H. Negoro, & K. Terada, ApJ 391 (1992) L21.
14. J.D. Scargle, ApJ 263 (1982) 835.
15. B.A. Vaughan & M.A. Nowak, ApJ 474 (1997) L43.
16. S. Miyamoto, S. Kitamoto, K. Mitsuda, & T. Dotani, Nature 336 (1988) 450.
17. M.C. Miller, ApJ 441 (1995) 770.
18. M.A. Nowak & B.A. Vaughan, MNRAS 280 (1996) 227.

We would like to acknowledge useful conversations with P. Michelson, M. van der Klis, D. Gruber, and K. Jahoda. This work was supported in part by NASA grants NAG 5-3225 and NAG 5-3310 (MAN), as well as NASA Grants NAG 5-2026, NAG 5-3239, NSF Grants AST91-20599, AST95-29175, INT95-13899, DARA grant 50 OR 92054, and by a travel grant to J.W. from the DAAD.